Spin-enhanced nanodiamond biosensing for ultrasensitive diagnostics

Benjamin S. Miller[1,2]*, Leonard Bezinge[1], Harriet D. Gliddon[1], Da Huang[1], Gavin Dold[1,3], Eleanor R. Gray[1], Judith Heaney[4], Peter J. Dobson[5], Eleni Nastouli[6], John J. L. Morton[1,3] & Rachel A. McKendry[1,2]*

1. *London Centre for Nanotechnology, University College London, 17-19 Gordon Street, London WC1H 0AH, United Kingdom.*
2. *Division of Medicine, University College London, Gower Street London WC1E 6BT, United Kingdom.*
3. *Department of Electronic & Electrical Engineering, University College London, London WC1E 7JE, United Kingdom.*
4. *Advanced Pathogens Diagnostic Unit, UCLH, London NW1 2BU, United Kingdom.*
5. *The Queens College, University of Oxford, OX1 4AW, United Kingdom.*
6. *Department of Virology, UCLH, London NW1 2BU, United Kingdom.*

The quantum spin properties of nitrogen-vacancy defects in diamond have diverse applications including quantum computing and communications[1], but nanodiamonds also have attractive properties for in vitro biosensing, including brightness[2], low cost[3], and selective manipulation of their emission[4]. Nanoparticle-based biosensors are vital for early disease detection, however, often lack the required sensitivity. Here we investigated fluorescent nanodiamonds as an ultra-sensitive label for in vitro diagnostics, using a microwave field to modulate emission intensity[5], and frequency-domain analysis[6] to separate the signal from background autofluorescence[7], which typically limits sensitivity. We focused on the common, low-cost lateral flow format as an exemplar, achieving detection limits of 8.2×10^{-19} M for a biotin-avidin model, 10^5-fold more sensitive than gold nanoparticles; and a use-case demonstration of single-copy detection of HIV-1 RNA with a short 10-minute isothermal amplification step, including a pilot using a clinical plasma sample with an extraction step. This ultra-sensitive quantum-diagnostics platform is applicable to numerous diagnostic test formats and diseases with the potential to transform early diagnosis, benefiting patients and populations.

32   Fluorescent nanodiamonds (FNDs) containing nitrogen-vacancy (NV) centres (defects

33   with optical transitions within the band gap) have received considerable attention as a spin

34   system for use as a qubit in quantum computing and communication, and for quantum

35   sensing[1,4,8,9]. Such applications stem from the ability of the NV^- spin state to be optically

36   initialised and read out, while being manipulated using DC and microwave magnetic fields.

37   FNDs also have attractive fluorescent properties: high quantum yield, non-blinking, no

38   photobleaching, stability, low cytotoxicity[2,10], available surface groups for bio-

39   functionalisation[11], and easy mass manufacture, such as from milling of high pressure, high

40   temperature diamond[3,12]. The sensing applications of NV centres[4] include magnetic field

41   quantification[13–15], temperature sensing[16,17], and biological labelling[2,18], the latter including

42   cellular imaging [19], drug delivery[20], and MRI contrast enhancement[21]. A key advantage of

43   negative NV centres (NV^-) is that their fluorescence can be selectively modulated by spin

44   manipulation[4] (neutral NV^0 centres cannot), allowing for signal separation for imaging in

45   high-background environments. This property has been used to improve the contrast for

46   imaging by modulating the fluorescence with microwaves[5,22], magnetic fields[23,24], or near-

47   infrared light[25]. Here, we investigated the use of FNDs for *in vitro* diagnostics.

48   Communicable diseases represent an enormous global health challenge,

49   disproportionately affecting poorer populations with limited access to healthcare[26]. At the

50   end of 2015, there were 36.9 million people living with HIV worldwide, of whom 9.4 million

51   (25%) were unaware of their HIV status[27]. Early diagnosis is crucial for effective treatment

52   and prevention, benefiting patients and populations. For example, UK patients starting

53   antiretroviral therapy for HIV following a late diagnosis saw a reduction in life expectancy of

54   over 12 years compared to those starting treatment with an earlier diagnosis[28]. The earliest

55   marker of HIV is viral RNA, detectable seven days before antigen and 16 days before

56   antibodies[29]. Point-of-care nucleic acid testing, therefore, offers the potential for earlier

57   diagnosis than either existing laboratory-based nucleic acid tests, or point-of-care protein

58   tests.

59   Rapid point-of-care tests have transformed access to disease testing in a variety of
60   community settings, including clinics, pharmacies and the home[30]. Among the most
61   common tests worldwide are paper microfluidic lateral flow assays (LFAs), with 276 million
62   sold in 2017 for malaria alone[31]. LFAs satisfy many of the REASSURED criteria[32] for
63   diagnostics, however, despite widespread use they are still limited by inadequate sensitivity
64   to detect the low levels of biomarkers necessary for early disease detection.

65   Fluorescent markers can be highly sensitive, but are practically limited by background
66   fluorescence from the sample, substrate, or readout technique. In the case of nitrocellulose
67   substrates used in LFAs, there is a significant background autofluorescence[7], which
68   inherently limits sensitivity. Various methods have been reported to reduce this effect, such
69   as membrane modification to reduce background fluorescence[33], exciting in the near-
70   infrared range and using upconverting nanoparticles[34], and time-gated detection using long-
71   persistent phosphors[35] to separate background fluorescence, which has a shorter lifetime.
72   These methods have shown ~10-fold improvements in sensitivity over gold nanoparticles,
73   limited by relatively low brightness.

74   Here we show the use of FNDs as a fluorescent label in an LFA format as a
75   demonstrator of their first use for *in vitro* diagnostics, taking advantage of their high
76   brightness and selective modulation. The use of a narrowband resonator allows for the low-
77   power generation of microwave-frequency electromagnetic fields, suitable for a point-of-
78   care device, to efficiently separate the signal from the background in the frequency domain
79   by lock-in[6] detection. We aimed, after characterisation, functionalisation, and optimisation,
80   to apply FND-based LFAs first to a model system, then to a molecular HIV-1 RNA assay to
81   demonstrate clinical utility.

82   **Results and discussion**

83   An illustration of the use of FNDs in LFAs is shown in Figure 1. FNDs can be used as
84   nanoparticle labels on nitrocellulose strips, undergoing a multiple step binding assay with
85   little user input to bind at the test line in the presence of the target nucleic acids. Once

86   immobilised, FND fluorescence can be modulated at a fixed frequency using a microwave

87   field, allowing them to be specifically detected and quantified.

88   **Figure 1: Schematic illustration of the use of FNDs in LFAs.** (a) Illustration of the concept of

89   fluorescent nanodiamonds (FNDs) in a lateral flow assay (LFA). The binding of DNA modifications

90   causes FNDs to be immobilised at the test line in a sandwich-format LFA. Inset is the atomic

91   structure of a NV⁻ centre, the origin of FND fluorescence. An omega-shaped stripline resonator

92   applies a microwave field over the LFA, modulating the fluorescence intensity. (b) A schematic

93   showing more detail of the principle. FNDs are immobilised at the test line in a sandwich structure in

94   the presence of dsDNA amplicons. Exciting at 550nm (green) produces fluorescence emission

95   centred at 675nm (red), imaged with a camera. An amplitude modulated microwave field, applied

96   by the resonator, selectively modulates the fluorescence of the immobilised FNDs at a set

97   frequency. This allows specific separation of the FND fluorescence from background fluorescence in

98   the frequency domain, to improve the signal-to-noise ratio.

99   **Microwave modulation of fluorescent nanodiamond emission on paper**

100   An energy level diagram of the NV⁻ centre, the origin of FND fluorescence, is shown in

101   Figure 2a. The triplet ground state is optically driven into an excited triplet state, which then

102   radiatively decays back to the ground states. Throughout the process, the electron spin

103   state ($m_s = 0, \pm1$) is conserved, however, the $m_s = \pm1$ excited state levels can decay into a

104   metastable 'dark' state with a corresponding reduction in fluorescence[4]. Resonant

105   microwave radiation drives electron spin population from the $m_s = 0$ to the $m_s = \pm1$ levels,

106   reducing fluorescence intensity. The microwave field was produced by a voltage-controlled

107   oscillator connected to an antenna, capacitively coupled to an omega-shaped stripline

108   resonator that provides a uniform peak field over the measurement area (the area of the

109   resonator).

110   Characterisation of the FND fluorescence and microwave field response was

111   undertaken on the nitrocellulose paper substrate. To investigate the FND fluorescence

112   intensity with microwave frequency on paper, a wideband resonator was used to perform

4

113   continuous-wave electron spin resonance spectroscopy, shown in Extended Data Figure 1a-

114   c. A plot of FND fluorescence over a wide frequency range is shown in Figure 2b, showing

115   two peaks at ΔE = 2.87GHz and $\Delta E\ast$ = 1.43GHz, corresponding to the triplet level splitting in

116   the ground and excited states, respectively. Figure 2c shows a narrowband resonator,

117   characterised in Extended Data Figure 1d-f, designed to have a resonant frequency at

118   2.87GHz with quality factor Q = 100, which induced a ~3–6% reduction in measured

119   fluorescence (Extended Data Figure 1f), varying linearly with the microwave input power in

120   dBm (see Extended Data Figure 1g-h).

121   FND fluorescence excitation and emission spectra are shown in Figure 2d. The

122   presence of NV⁻ centres is indicated by presence of the zero-phonon line (ZPL) at ~640nm.

123   Using an amplitude-modulated microwave field to specifically vary FND fluorescence at a

124   fixed frequency allows for the application of a computational lock-in algorithm[6] (shown

125   schematically in Extended Data Figure 2a), to selectively extract signals at the reference

126   frequency. This lock-in analysis, shown by Igarashi et al.[5], separates the periodic FND

127   fluorescence from the non-periodic background fluorescence, caused by nitrocellulose

128   autofluorescence, thus improving sensitivity.

129   The fluorescence modulation is shown in Figure 2e & f. Figure 2e shows pixel variation

130   over time: the test line, where FNDs are immobilised, has a high variance compared to the

131   background, which does not modulate and has low variance. The time-series is shown in

132   Figure 2f (top) – a square-wave 4Hz amplitude-modulated microwave field modulates the

133   fluorescence intensity. Applying the lock-in algorithm over a small frequency range gave the

134   plot in Figure 2f (bottom), an absolute sinc function, the Fourier transform of a square

135   pulse. The maximum response is shown when the reference frequency matches the

136   modulation frequency at 4Hz. The optimisation of modulation frequency, sampling

137   frequency, exposure time and measurement time are shown in Extended Data Figures 2b-e.

138   Microwave generation was miniaturised using a voltage-controlled oscillator, amplifier and

139   custom power and timing circuit (65mm x 38mm, Extended Data Figure 2f-g).

Figure 2: Microwave modulation of FNDs on paper. (a) Energy level diagram of a NV⁻ centre. Splitting in the ground and excited states is labelled as ΔE and $\Delta E*$, respectively. (b) The variation FND fluorescence under different frequency microwave fields, showing dips at energies ΔE and $\Delta E*$. Some peak splitting is observed around the centre frequency due to a ~3G magnetic field generated by the resonator (measured with a Gaussmeter). (c) A microscope image of the omega-shaped stripline resonator used to produce a uniform field at 2.87GHz. (d) Excitation and emission spectra of FNDs. The green shaded area shows the filtered excitation light used. The emission spectrum area is reduced under the application of the microwave field. (e) The pixel variation at the test line (with immobilised FNDs) of an LFA strip under an amplitude-modulated microwave field. (f) The variation of mean fluorescence intensity over time under the application of the same amplitude-modulated field (top). Applying at lock-in algorithm over a range of frequencies gives a sinc function peaking at the modulation frequency (bottom).

Fundamental limits: biotin-avidin model

Following this fluorescence characterisation and optimisation of the modulation parameters, FNDs were functionalised with biomolecules for incorporation into LFAs. FNDs with a polyglycerol (PG) layer were used, as the hydrophilic layer reduces non-specific binding to the nitrocellulose[36] (Extended Data Figure 3a), a key limitation of LFA sensitivity. Three sizes of FND-PG (dynamic light scattering shown in Extended Data Figure 3b) were functionalised with antibodies via activation of the PG alcohol groups with disuccinimidyl carbonate (DSC)[37], as shown in Extended Data Figure 3c. Characterisation by scanning electron microscopy, dynamic light scattering and Fourier transform infrared (FTIR) spectroscopy in Extended Data Figure 3d-i showed successful conjugation, with no significant aggregation upon functionalisation and increases in size consistent with the size of the conjugants[38,39]. The number of active binding sites on the FND surface (600nm diameter) was subsequently quantified using quantitative PCR, as described in Methods and shown in Extended Data Figure 4. The measured value of 4,300 active binding sites per FND is consistent with geometric calculations of the number of antibodies that could bind.

167   The fundamental limit of detection (LOD) of FND-based LFAs was investigated using a
168   model biotin-avidin interaction. A serial dilution of BSA-biotin-functionalised FNDs was run
169   on LFA strips with a poly-streptavidin test line, so bound directly (rather than in a sandwich
170   formation), shown schematically in Figure 3a. This high affinity along with the flow rate and
171   high binding capacity of nitrocellulose ensures that the residency time of the FNDs at the
172   test line is much longer than the binding time of biotinylated FNDs to the streptavidin
173   (Extended Data Figure 5a-b). This implies that all the FNDs bind at the test line, making it
174   ideal for benchmarking the best-case sensitivity, and comparing with other nanomaterials.
175   The LODs were quantified for three different particle core diameters: 120, 200 and 600nm.

176   The resulting LFA test line fluorescence signals were analysed using lock-in analysis,
177   and by conventional intensity analysis (measuring the intensity difference between the test
178   line and background), and compared with gold nanoparticles, commonly used in LFAs[40]. The
179   signal-to-blank ratios (SBRs) were plotted against concentration in Figure 3b for 600nm
180   FNDs. Each dilution series was fitted to a simple linear regression, and the LOD was defined
181   as the intersection of the lower 95% confidence interval of the linear fit with the upper 95%
182   confidence interval of the blanks[41]. Figure 3c demonstrates this comparison, with images of
183   the test lines at various concentrations (top). Below (Figure 3c bottom) are time-series of
184   the fluorescence modulation at each FND concentration, showing that signal modulation
185   can be measured well below the concentration at which there is a visible test line.

186   LODs were 200aM, 46aM, and 820zM for particles of 120, 200 and 600nm diameters,
187   respectively (Extended Data Figure 5d). The larger particles gave the best LODs because the
188   lock-in amplitude scales with the fluorescence modulation intensity, which in turn scales
189   with the number of NV$^-$ centres. The number of NV$^-$ centres per particle scales with the
190   volume, so the LOD should scale with diameter cubed. Additionally, surface effects reduce
191   the fluorescence of NV$^-$ centres close to the surface, so a larger volume to surface ratio
192   should increase fluorescence intensity.

7

193   LODs using 600nm FNDs were 820zM and 83aM for lock-in and conventional analysis

194 respectively, yielding a 620-fold improvement in signal-to-background ratio, giving a 100-

195 fold improvement in the LOD. This increases to an 810-fold improvement in signal-to-

196 background ratio using 120nm FNDs, giving a 380-fold improvement in the LOD.

197   This fundamental LOD of 820zM corresponds to 0.5 particles/µL, or just 27 particles in

198 a 55µL sample. For comparison, the same experiment was performed with 50nm gold

199 nanoparticle labels, commonly used in LFAs[40] due to their ease-of-functionalisation and

200 strong light absorption. 600nm FNDs were five orders of magnitude more sensitive. Useful

201 gold nanoparticle sizes on LFAs are also limited by the broadening of the plasmonic peak,

202 whilst larger FNDs become brighter. Due to the low numbers of particles detected, the LODs

203 of biological assays are expected to be limited by non-specific binding and equilibrium

204 considerations, rather than the fundamental sensitivity of FNDs.

205 **Figure 3: Characterising the fundamental limit of detection using biotin-avidin binding of FNDs on**

206 **LFAs.** (a) Schematic of the assay – FNDs functionalised with BSA-biotin were run on streptavidin-

207 printed LFA strips, binding directly to the test line. The arrow shows the flow direction. (b) A dilution

208 series of 600nm FNDs was measured by both lock-in analysis and conventional intensity analysis,

209 and compared to 50nm gold nanoparticles, giving LODs of 820zM, 83aM, and 81fM, respectively.

210 Lock-in analysis gave a 100-fold improvement over conventional intensity analysis, and a 98,000-fold

211 improvement over gold nanoparticles. Error bars show standard deviations of three technical

212 replicates (n_T = 3), and three measurement replicates (n_M = 3) for each sample. (c) An illustration of

213 this comparison, with example images at various concentrations (above), and intensity-time plots

214 (below), showing that a periodic signal is still evident after the test line is no longer visible in the

215 images.

216 **Single-copy detection of HIV-1 RNA with isothermal amplification**

217 This technology platform was then applied to a proof-of-concept assay, detecting DNA

218 amplicons. The assay is based on a reverse transcriptase-recombinase polymerase

219 amplification (RT-RPA) reaction for the detection of HIV-1 RNA, which is performed with

220   modified primers to form a sandwich structure on the nitrocellulose, as shown in Figure 4a.

221   Following assay optimisation, shown in Extended Data Figures 6-8 and described in

222   methods, LFAs were performed with serial dilutions of RT-RPA products using three particle

223   sizes (120, 200 and 600nm). The initial aim was to determine the sensitivity of the detection

224   system, rather than the amplification step, so the amplicon concentration used was

225   measured post-amplification. Resulting plots of SBR against amplicon concentration are

226   shown in Figure 4b, and fitted to the Langmuir adsorption isotherm model (Methods

227   Equation 6). The LODs were measured as 9.0, 7.5 and 3.7fM for 120, 200 and 600nm

228   diameter FNDs, respectively. The 3.7fM LOD with 600nm particles corresponds to 2,200

229   copies/µL, or 1.1×10^5 copies in total (190zmol of DNA).

230   A model 'amplicon' (described in methods and characterised in Extended Data Figure

231   9a-b) was used for a comparison of the 600nm particles with 40nm gold nanoparticles. The

232   resulting LODs, plotted in Extended Data Figure 9c, show that FNDs give a ~7,500-fold

233   improvement over 40nm gold nanoparticles. The ~13-fold reduction in improvement over

234   gold nanoparticles compared to the biotin-avidin model is due to non-specific binding. The

235   blanks in the DNA assay have the same FND concentration as the positives, whereas the

236   biotin-avidin assay has 'true blanks' (only running buffer). The resulting small lock-in

237   amplitude in the blanks is ~13-fold higher than a 'true blank' signal (noise), showing no

238   significant difference from the blanks from the biotin-avidin assay multiplied by this factor

239   of 13 (the two-tailed *t*-test *P* value= 0.33).

240   This level of sensitivity from the FND labelling means that a short amplification step

241   before adding to the LFA could lead to single-copy detection, with typical amplification

242   factors for isothermal RPA of 10^4 in 10min[42]. This was subsequently demonstrated by

243   performing 10min (37 °C) RT-RPA reactions on serial dilutions of HIV-1 transcript RNA,

244   before adding a 6X running buffer solution to the purified products, and running on LFAs as

245   previously. The resulting SBRs are plotted against RNA input copy number in Figure 4c,

246   showing a LOD of 1copy. Positive results were achieved down to a single RNA copy.

247   Statistical analysis of the lock-in amplitudes (analysis of variance) is shown in Extended Data

248 Figure 10a-c. Due to the 10-minute amplification time, all concentrations ≥1copy reach the

249 saturation signal, so a qualitative yes/no result is given. The variation of SBR with

250 amplification time is shown in Extended Data Figure 10d, where single-copy reactions were

251 run for different times. A detectable signal was observed after a 7-minute amplification

252 time. The sensitivity of the FNDs conveys improved LODs in shorter amplification times

253 compared to previous work with RPA using gold nanoparticles[43–46]. In addition, a proof-of-

254 concept clinical sample (UCLH clinical standard, 4 × 10^4 copies/µL) was successfully

255 detected. This involves the addition of an RNA extraction step, shown in Figure 4d, which

256 would need to be adapted to the point-of-care. RPA has been shown to be relatively robust

257 to complex samples, but this remains a major challenge for the field of nucleic acid

258 testing[47]. The positive clinical standard had a mean SBR of ~19 compared to the negative

259 plasma control.

260   In order to demonstrate the suitability of this system for rapid, early disease

261 detection, a small proof-of-concept was performed using a seroconversion panel of thirteen

262 samples taken over six weeks spanning the initial stages of an HIV-1 infection. Extended

263 Data Figure 10e shows that RNA is detected as early as with the RT-PCR gold standard,

264 giving positive results for 6/7 RT-PCR-positive, and 0/6 RT-PCR-negative samples. This is a

265 preliminary study and further optimisation with clinical samples and a larger study is

266 required to precisely ascertain the clinical sensitivity.

267 **Figure 4: Single-copy detection of HIV-1 RNA on LFAs using RT-RPA and FNDs.** (a) A schematic of

268 the assay. Digoxigenin and biotin-modified primers were used in a RT-RPA reaction to produce

269 labelled amplicons, which bind to anti-digoxigenin-functionalised FNDs, and streptavidin printed test

270 lines on the LFA strips, forming a sandwich structure in the presence of amplicons. (b) Dilution series

271 of amplicons were run on LFAs for three different particles sizes (120, 200 and 600nm). Serial

272 dilutions were plotted (dots with error bars showing standard deviations, n_T = 3-9, n_M = 3), and fitted

273 to the Langmuir adsorption model in Methods Equation 6. Limits of detection for 120, 200 and

274 600nm diameter FNDs were 9.0, 7.5 and 3.7fM respectively. * marks the lowest concentrations for

275 each particle size that are significantly different from the blanks at the 95% confidence level,

276 calculated by ANOVA. (c) Serial dilutions of HIV-1 RNA copies were amplified with RT-RPA (10min),

277   purified, and run on LFAs with 600nm FNDs. The RNA concentration was plotted against signal-to-
278   blank ratio (dots showing the mean, error bars showing standard deviations, and crosses showing
279   individual measurements), with four experimental replicates (n_E = 4), and three measurement
280   replicates (n_M = 3) for each sample. Single-copy sensitivity was achieved. (d) The system was applied
281   to a proof-of-concept positive clinical sample (UCLH clinical standard), and negative human plasma
282   control, giving a mean SBR of ~19 and a *P* value between the negative and positive clinical samples
283   of 8×10^{-13} with a *t* value of -19.3 from an unpaired one-tailed *t*-test.

284   **Conclusions**

285   Herein, we have shown the use of FNDs as an ultra-sensitive fluorescent label for *in vitro*
286   diagnostic assays, using microwave-based spin manipulation to increase the signal-to-
287   background ratio, and therefore sensitivity. The system was demonstrated in an LFA format
288   with two assays. Using a biotin-avidin model, a fundamental LOD of 0.5particles/µL was
289   measured, five orders of magnitude more sensitive than gold nanoparticles, with the caveat
290   of increased cost due to the need for a fluorescence reader (see Supplementary Table 1),
291   but the advantage of data capture (compared to visual interpretation). Applying FNDs to a
292   sandwich assay for oligonucleotide detection, single-copy sensitivity was achieved for the
293   detection of RNA with a 10min RT-RPA step, using 600nm FNDs. The sensitivity of the FND
294   detection system (LOD of 2,200 copies/µL with RT-RPA amplicons, measured post
295   amplification) meant a short amplification time is possible whilst achieving higher sensitivity
296   than has been previously demonstrated with other nanomaterials[45,48], making the test more
297   suitable for point-of-care applications. A comparison with other fluorescence-based
298   amplicon detection on LFAs is shown in Supplementary Table 2. The system was also
299   demonstrated with HIV-1-positive and negative clinical samples with the addition of an RNA
300   extraction step.

301   There are remaining challenges to translate this exemplar RNA detection assay
302   towards a rapid point-of-care test meeting the REASSURED criteria[32], summarised in
303   Supplementary Table 3. The incorporation of the amplification step on the LFA strip[45] is a
304   major challenge, along with sample processing and RNA extraction in resource-limited

305　settings[47], and removing the wash step. However, the sensitivity of this transduction

306　technique means there is leeway for sensitivity reductions, whilst retaining clinical

307　relevance: we have demonstrated single-copy detection with a 10min RT-RPA step, up to

308　50-fold greater sensitivity than the World Health Organisation viral suppression threshold of

309　1,000 copies/mL[49]. It is also flexible and easily translatable to other assays: amplification

310　methods using modified primers, including existing PCR assays, by changing only the

311　primers; direct detection by hybridisation of complementary modified probe sequences to a

312　molecular target; or protein detection in a sandwich assay using modified antibodies. In

313　order to demonstrate this, detection of the HIV-1 capsid protein using FNDs on paper was

314　evaluated, shown in Extended Data Figure 11, giving a LOD of 120fM. FNDs are also

315　applicable to a range of other *in vitro* diagnostic test formats. In addition, due to the long

316　fluorescence lifetimes of NV centres[50] compared to nitrocellulose[7], time-gated fluorescence

317　measurements could be used to further improve FND-based LFA sensitivity.

318　　　The low power consumption (0.25W microwave power), optical readout, and

319　potential portability of this technique make it suitable for ultra-sensitive diagnosis and

320　monitoring in low-resource settings, with a portable fluorescence reader or smartphone-

321　based device including microwave modulation. The nature of lock-in readout makes it

322　robust to background light, minimising sensitivity losses when moving from a microscope to

323　such a portable device. FNDs on paper microfluidics offer a sensitive, robust labelling and

324　readout method for *in vitro* disease diagnostics.

325　**References**

326　1. Childress, L. & Hanson, R. Diamond NV centers for quantum computing and quantum

327　networks. *MRS Bulletin* **38**, 134–138 (2013).

328　2. Mochalin, V. N., Shenderova, O., Ho, D. & Gogotsi, Y. The properties and applications of

329　nanodiamonds. *Nature Nanotechnology* **7**, 11–23 (2012).

3. Boudou, J.-P. *et al.* High yield fabrication of fluorescent nanodiamonds. *Nanotechnology* **20**, 235602 (2009).

4. Schirhagl, R., Chang, K., Loretz, M. & Degen, C. L. Nitrogen-Vacancy Centers in Diamond: Nanoscale Sensors for Physics and Biology. *Annual Review of Physical Chemistry* **65**, 83–105 (2014).

5. Igarashi, R. *et al.* Real-time background-free selective imaging of fluorescent nanodiamonds in vivo. *Nano Letters* **12**, 5726–5732 (2012).

6. Leis, J., Martin, P. & Buttsworth, D. Simplified digital lock-in amplifier algorithm. *Electronics Letters* **48**, 259 (2012).

7. Shah, K. G. & Yager, P. Wavelengths and Lifetimes of Paper Autofluorescence: A Simple Substrate Screening Process to Enhance the Sensitivity of Fluorescence-Based Assays in Paper. *Analytical Chemistry* **89**, 12023–12029 (2017).

8. Childress, L. *et al.* Coherent Dynamics of Coupled Electron and Nuclear Spin Qubits in Diamond. *Science* **314**, 281–285 (2006).

9. Chang, H.-C., Hsiao, W. W.-W. & Su, M.-C. *Fluorescent Nanodiamonds* (John Wiley & Sons, Ltd, Chichester, UK, 2018).

10. Yu, S. J., Kang, M. W., Chang, H. C., Chen, K. M. & Yu, Y. C. Bright fluorescent nanodiamonds: No photobleaching and low cytotoxicity. *Journal of the American Chemical Society* **127**, 17604–17605 (2005).

11. Shenderova, O. A. & McGuire, G. E. Science and engineering of nanodiamond particle surfaces for biological applications (Review). *Biointerphases* **10**, 030802 (2015).

12. Chang, Y. R. *et al.* Mass production and dynamic imaging of fluorescent nanodiamonds. *Nature Nanotechnology* **3**, 284–288 (2008).

353 13. Maze, J. R. *et al.* Nanoscale magnetic sensing with an individual electronic spin in diamond.
354   *Nature* **455**, 644–647 (2008).

355 14. Balasubramanian, G. *et al.* Nanoscale imaging magnetometry with diamond spins under
356   ambient conditions. *Nature* **455**, 648–651 (2008).

357 15. Tetienne, J. P. *et al.* Magnetic-field-dependent photodynamics of single NV defects in
358   diamond: An application to qualitative all-optical magnetic imaging. *New Journal of Physics*
359   **14** (2012).

360 16. Acosta, V. M. *et al.* Temperature Dependence of the Nitrogen-Vacancy Magnetic Resonance
361   in Diamond. *Physical Review Letters* **104**, 070801 (2010).

362 17. Hsiao, W. W. W., Hui, Y. Y., Tsai, P. C. & Chang, H. C. Fluorescent Nanodiamond: A Versatile
363   Tool for Long-Term Cell Tracking, Super-Resolution Imaging, and Nanoscale Temperature
364   Sensing. *Accounts of Chemical Research* **49**, 400–407 (2016).

365 18. Vaijayanthimala, V. & Chang, H.-C. Functionalized fluorescent nanodiamonds for biomedical
366   applications. *Nanomedicine (London, England)* **4**, 47–55 (2009).

367 19. Fu, C.-C. *et al.* Characterization and application of single fluorescent nanodiamonds as
368   cellular biomarkers. *Proceedings of the National Academy of Sciences* **104**, 727–732 (2007).

369 20. Chang, B. M. *et al.* Highly fluorescent nanodiamonds protein-functionalized for cell labeling
370   and targeting. *Advanced Functional Materials* **23**, 5737–5745 (2013).

371 21. Waddington, D. E. *et al.* Nanodiamond-enhanced MRI via in situ hyperpolarization. *Nature*
372   *Communications* **8**, 1–8 (2017).

373 22. Hegyi, A. & Yablonovitch, E. Molecular imaging by optically detected electron spin
374   resonance of nitrogen-vacancies in nanodiamonds. *Nano Letters* **13**, 1173–1178 (2013).

23. Sarkar, S. K. *et al.* Wide-field in vivo background free imaging by selective magnetic modulation of nanodiamond fluorescence. *Biomedical Optics Express* **5**, 1190 (2014).

24. Chapman, R. & Plakhoitnik, T. Background-free imaging of luminescent nanodiamonds using external magnetic field for contrast enhancement. *Optics Letters* **38**, 1847 (2013).

25. Doronina-Amitonova, L., Fedotov, I. & Zheltikov, A. Ultrahigh-contrast imaging by temporally modulated stimulated emission depletion. *Optics Letters* **40**, 725 (2015).

26. Bhutta, Z. A., Sommerfeld, J., Lassi, Z. S., Salam, R. A. & Das, J. K. Global burden, distribution, and interventions for infectious diseases of poverty. *Infectious Diseases of Poverty* **3**, 21 (2014).

27. UNAIDS. Global HIV & AIDS statistics - 2018 fact sheet. Tech. Rep. (2018).

28. May, M. *et al.* Impact of late diagnosis and treatment on life expectancy in people with HIV-1: UK Collaborative HIV Cohort (UK CHIC) Study. *BMJ* **343**, d6016–d6016 (2011).

29. Gray, E. R. *et al.* p24 revisited: a landscape review of antigen detection for early HIV diagnosis. *AIDS* **32**, 2089–2102 (2018).

30. Price, C. P. Regular review: Point of care testing. *BMJ* **322**, 1285–1288 (2001).

31. World Health Organization. World Malaria Report. Tech. Rep. (2018).

32. Land, K. J., Boeras, D. I., Chen, X. S., Ramsay, A. R. & Peeling, R. W. REASSURED diagnostics to inform disease control strategies, strengthen health systems and improve patient outcomes. *Nature Microbiology* **4**, 46–54 (2019).

33. Walter, J. G. *et al.* Protein microarrays: Reduced autofluorescence and improved LOD. *Engineering in Life Sciences* **10**, 103–108 (2010).

34. Kim, J. *et al.* Rapid and background-free detection of avian influenza virus in opaque sample using NIR-to-NIR upconversion nanoparticle-based lateral flow immunoassay platform. *Biosensors and Bioelectronics* **112**, 209–215 (2018).

35. Paterson, A. S. *et al.* A low-cost smartphone-based platform for highly sensitive point-of-care testing with persistent luminescent phosphors. *Lab Chip* **17**, 1051–1059 (2017).

36. Boudou, J. P., David, M. O., Joshi, V., Eidi, H. & Curmi, P. A. Hyperbranched polyglycerol modified fluorescent nanodiamond for biomedical research. *Diamond and Related Materials* **38**, 131–138 (2013).

37. Hermanson, G. T. Zero-Length Crosslinkers. *Bioconjugate Techniques* 259–273 (2013).

38. Gonzalez Flecha, F. L. & Levi, V. Determination of the molecular size of BSA by fluorescence anisotropy. *Biochemistry and Molecular Biology Education* **31**, 319–322 (2003).

39. Reth, M. Matching cellular dimensions with molecular sizes. *Nature Immunology* **14**, 765–767 (2013).

40. Ngom, B., Guo, Y., Wang, X. & Bi, D. Development and application of lateral flow test strip technology for detection of infectious agents and chemical contaminants: a review. *Analytical and Bioanalytical Chemistry* **397**, 1113–1135 (2010).

41. Armbruster, D. A. & Pry, T. Limit of blank, limit of detection and limit of quantitation. *The Clinical biochemist. Reviews / Australian Association of Clinical Biochemists* **29 Suppl 1**, 49–52 (2008).

42. Daher, R. K., Stewart, G., Boissinot, M. & Bergeron, M. G. Recombinase polymerase amplification for diagnostic applications. *Clinical Chemistry* **62**, 947–958 (2016).

43. Lillis, L. *et al.* Cross-subtype detection of HIV-1 using reverse transcription and recombinase polymerase amplification. *Journal of Virological Methods* **230**, 28–35 (2016).

419 44. Crannell, Z. A., Rohrman, B. & Richards-Kortum, R. Equipment-free incubation of

420   recombinase polymerase amplification reactions using body heat. *PLoS ONE* **9**, 1–7 (2014).

421 45. Rohrman, B. A. & Richards-Kortum, R. R. A paper and plastic device for performing

422   recombinase polymerase amplification of HIV DNA. *Lab on a Chip* **12**, 3082 (2012).

423 46. Boyle, D. S., Lehman, D. A. & Lillis, L. Rapid Detection of HIV-1 Proviral DNA for Early Infant

424   Diagnosis Using Rapid Detection of HIV-1 Proviral DNA for Early Infant Diagnosis. *mBio* **4**,

425   00135–13 (2013).

426 47. Dineva, M. A., Mahilum-Tapay, L. & Lee, H. Sample preparation: a challenge in the

427   development of point-of-care nucleic acid-based assays for resource-limited settings. *The*

428   *Analyst* **132**, 1193 (2007).

429 48. Jauset-Rubio, M. *et al.* Ultrasensitive, rapid and inexpensive detection of DNA using paper

430   based lateral flow assay. *Scientific Reports* **6**, 37732 (2016).

431 49. Phillips, A. *et al.* Sustainable HIV treatment in Africa through viral-load-informed

432   differentiated care. *Nature* **528**, S68–S76 (2015).

433 50. Kuo, Y., Hsu, T.-Y., Wu, Y.-C., Hsu, J.-H. & Chang, H.-C. Fluorescence lifetime imaging

434   microscopy of nanodiamonds in vivo. *Advances in Photonics of Quantum Computing,*

435   *Memory, and Communication VI* **8635**, 863503 (2013).

436 **Acknowledgements**

Author Contributions

447 B.S.M., and R.A.M. conceived the research and led the study; P.J.D advised on nanodiamonds

448 and J.J.L.M. on microwave modulation. B.S.M. showed the initial proof-of-concept; B.S.M. and

449 L.B. designed and optimised the lock-in analysis, functionalisation and LFA design; B.S.M., L.B.

450 and D.H. performed all the FND LFA experiments; H.D.G. designed, optimised and performed

451 RT-RPA assays including primer design and template generation; D.H. adapted and performed

452 RT-RPA assays and purification; J.J.L.M. and G.D. designed the microwave delivery including

453 resonators; E.R.G. performed clinical RNA extraction, and advised on virology including primer

454 design; J.H. performed qPCR on seroconversion panel; E.N. provided clinical expertise; B.S.M.

455 and E.R.G. designed and performed binding site quantification experiments; B.S.M., L.B. and

456 R.A.M. drafted the manuscript; and all authors reviewed and revised the manuscript.

Competing Interests

458 The authors declare the following competing financial interest(s): B.S.M., L.B., G.D., P.J.D.,

459 J.J.L.M. and R.A.M. are inventors on the UK patent application number 1814532.6.

Correspondence

461 Correspondence and requests for materials should be addressed to R. A. McKendry (email:

462 r.a.mckendry@ucl.ac.uk).

Methods

464 **Resonator design.** CST Studio Suite 2015 (Dassault Systems) was used to create a 3D model

465 of the resonator design, solving Maxwell's equations over a sweep of microwave

18

466   frequencies to determine reflected and absorbed power. The design was based on copper

467   patterned on a printed circuit board, using Rogers 4003C substrate for low dielectric loss at

468   microwave frequencies. The top side had an interdigitated capacitor and a capacitor-

469   inductor omega-shaped loop, and the bottom had a ground plane. The dimensions of these

470   components were varied iteratively to maximise the absorption at 2.87GHz and ensure an

471   impedance of 50Ω for coupling to the frequency generator. The final design was exported

472   as a 2D CAD file.

473   **Preparation of functionalised FNDs.** PG-functionalised FNDs were conjugated to Abs using

474   DSC as shown in Extended Data Figure 3c. DSC activates hydroxyl surface groups to form

475   succinimidyl carbonates, which can then react with antibodies to form stable carbamate or

476   urethane bonds[37].

477   In a typical synthesis, 100µL FND-PG (1mg mL^{-1}, Adamas Nanotechnologies, high brightness

478   120nm core + 20nm PG FND NDNV140nmHiPG2mg) were centrifuged at 21,130rcf for

479   7.5min to condense the particles into a pellet. The supernatant was then removed and the

480   FNDs were resuspended in anhydrous N,N-Dimethylformamide (DMF, 99.8%, Sigma-

481   Aldrich). After resuspension in DMF, the colloidal solution was sonicated for 5min in an

482   ultrasonic bath. The washing and sonication steps were repeated three times to remove

483   water. After the last centrifugation, the particles were resupended in 100µL of a 50mg mL^{-1}

484   solution of DSC (≥95%, Sigma-Aldrich) in DMF and placed in a thermoshaker for 3.5h at

485   300rpm and room temperature. Excess reagents were removed by three cycles of

486   centrifugation and resuspension in DMF (as described above). After the third centrifugation,

487   the particles were resuspended in 100µL deionised water.

488   Depending on the desired surface functionalisation, 13.7µL of anti-digoxigenin antibodies

489   (1mg mL^{-1}, Abcam plc, ab76907) or 6.8µL BSA-biotin (2mg mL^{-1} in deionised water, Sigma-

490   Aldrich) were added to the activated FNDs. The mixture was placed in a thermoshaker

491   overnight for 15h at 300rpm and room temperature. The remaining succinimidyl

492   carbonates were quenched by adding of 10µL of Tris-HCl pH 7.5 (1M, Thermo Fisher

493   Scientific). After 30min, the unbound reagents were removed by three cycles of

494   centrifugation and resuspension in deionised water (100μL) and stored in 100μL of PBS with

495   0.1wt% BSA.

496   After functionalisation, the FND concentrations were quantified by fluorescence intensity,

497   as this remains unchanged during the functionalisation reactions: the fluorescence

498   originates from the atomic structure of the FNDs, so is unaffected by surface modifications.

499   This was carried out by performing a serial dilution of the FND stock solution (of know mass

500   concentration, c_P, of 1mg mL^{-1} based on manufacturers specifications) and using a

501   spectrophotometer to measure the fluorescence compared to the functionalised-FND

502   solution. A linear regression was fitted to the fluorescence intensity of the serial dilution of

503   the stock FND solution against FND concentration and interpolated to calculate the mass

504   concentration of the functionalised particles. Examples of this for the three different

505   particle sizes are shown in Extended Data Figure 5c. This was converted to molar

506   concentration (C_P) using the diameter (d), density of diamond (ρ), and Avogadro constant

507   (N_A), shown in Methods Equation 1:

$$C_P(\text{M}) = \frac{c_P(\text{mg mL}^{-1})}{d^3(\text{nm}^3)} \cdot \frac{10^3}{\frac{\pi}{6} \cdot \rho(\text{mg nm}^{-3}) \cdot N_A(\text{mol}^{-1})} \tag{1}$$

508   Characterisation of Nanoparticles. Excitation spectra of the FNDs were acquired with a

509   fluorescence microplate reader (SpectraMax i3, Molecular Devices LLC) and served as a

510   reference to estimate the final FND concentration by comparison of the fluorescence

511   intensity with the stock solution. Emission spectra were recorded with a spectrometer

512   (SPM-002, Photon Control) with a 500nm LED light source (pE-4000, CoolLED). FTIR

513   spectroscopy was performed by conjugating particles as described above, and storing in

514   deionised water (maximum of 2 days), before centrifuging at 21,130rcf to condense the

515   particles into a pellet and removing as much supernatant as possible to form a paste. This

516   paste was pipetted onto the spectrometer (Bruker, Alpha). Three measurements of each

517   sample were taken using 16 reads per measurement. Dynamic light scattering data and zeta

518   potentials were measured with a Zetasizer (Zeta Sizer Nanoseries, Malvern Instruments Ltd)

519   using a 150-fold dilution of the FNDs. The resulting number plots were fitted to the skewed

520   exponential in Methods Equation 2 to find the peak diameter.

$$N(x) = \frac{\exp\left(\frac{-(x-\mu)^2}{2\sigma^2}\right)\operatorname{erfc}\left(\frac{-\alpha(x-\mu)}{\sqrt{2}\sigma}\right)}{\sqrt{2\pi}\sigma} \tag{2}$$

521   where N is the number fraction, x is the diameter, μ is the mean of the diameter

522   distribution, σ is the standard deviation, and α is the skew parameter.

523   **Quantification of antibody binding sites on FND surface.** In order to quantify the number

524   of active antibody binding sites on the surface, an assay similar to PCR-ELISA and Kim et al.[51]

525   was developed. 300µL FNDs were functionalised with anti-DIG antibodies, as described in

526   Methods, except the final suspension was in DNase/RNase-free distilled water (Thermo

527   Fisher UltraPure) rather than storage buffer, and the particles were concentrated 5-fold (to

528   5pM, 60µL). The suspension was subsequently split in half for a positive sample and a

529   negative control, and 6µL of a 6X running buffer solution was added to each, to a final

530   concentration of 1X running buffer (5% milk + 0.05% Empigen in water). A large excess of a

531   DIG-modified DNA sequence (0.9µM final concentration) was added to the positive sample,

532   and the same excess of the same DNA sequence, but with no DIG modification was added

533   to the negative control. A short DNA sequence (82bp) was used to avoid the bound DNA

534   blocking available sites on the FND surface. The DIG-DNA was left to bind to the FND-Ab for

535   2h. After binding, each solution was diluted to 400µL in DNase/RNase-free distilled water

536   before centrifuging at 376rcf for 2min and removing the supernatant. This washing was

537   repeated four times to remove excess DNA, with the final suspension in 150µL 100µg mL^{-1}

538   salmon sperm DNA solution (Thermo Fisher UltraPure).

539   Quantitative PCR (qPCR) was then performed on the final suspensions. The template,

540   primers and probe sequences are listed in Extended Data Figure 8d (assay taken from

541   Besnier et al.[52]). The master mix was the TaqMan Fast Virus 1-Step Master Mix (Thermo

21

542   Fisher) with primers at 300nM and the probe at 150nM, and 4µL of sample in a total

543   volume of 15µL. The standard was constructed from serial dilutions of the pHRSIN-CSGW

544   plasmid[53]. The qPCR was performed by an Applied Biosystems 7500 Real-Time PCR System

545   (Thermo Fisher), and the copy numbers quantified by the 7500 software (v2.0.6). The FND

546   concentrations in the final suspensions were measured as described in Methods. Dividing

547   the DNA copy number by the FND number gave the number of active binding sites per FND.

548   **Target Amplification by Recombinase Polymerase Amplification.** *RNA template generation*:

549   The template was designed using an alignment of 2929 clinical isolates of HIV-1 from the

550   Los Alamos HIV Sequence Database[54] to identify conserved areas. The alignment was

551   mapped to the Dr Michael Edelstein using Geneious Software (version 10.0.6) and a highly

552   conserved region of 229 bp (1573–1801 bp from HXB2) selected to design five forward and

553   five reverse primers to be tested in RPA primer selection. Starting from a R9BALΔEnv

554   plasmid (a gift from Greg Towers, UCL), DNA template was produced by polymerase chain

555   reaction amplification of the 1,503bp template sequence using the Phusion High-Fidelity

556   PCR Kit (New England Biolabs). Primer sequences used are shown in Extended Data Figure

557   8d. The thermocycling was performed at 98 °C for 30s, then 30 cycles of: 98 °C for 10s, 65 °C

558   for 20s, 72 °C for 25s, and a final extension of 72 °C for 10min. The DNA was then

559   transcribed to RNA using the MEGAscript T7 Transcription Kit (Invitrogen) and purified using

560   MEGAclear Transcription Clean-Up Kit (Invitrogen), following the manufacturer's

561   instructions. The concentration of RNA template was measured via Qubit RNA HS assay kit

562   (Invitrogen) with the Qubit 4 Fluorometer.

563   *RT-RPA reaction (amplicon serial dilution)*: RT-RPA assay was performed on a 1.5kb HIV-1 *in*

564   *vitro* transcribed RNA template. Optimisation of the assay is shown in Extended Data Figure

565   8. RT-RPA of the template was performed using TwistAmp Exo Reverse Transcription Kit

566   (TwistDx), following the manufacturer's instructions. The reaction time was 30min at 37 °C

567   shaking at 200rpm in an incubator (New Brunswick Innova 42). Nucleic acid sequences are

568   listed in Extended Data Figure 8d, including a fluorescent probe. During amplification,

569   exonuclease cuts the tetrahydrofuran, releasing the fluorescent tag (FAM) from the

22

570   quencher, producing a quantitative signal. The resulting RPA products were incubated with

571   RNAse A (QIAGEN) for 2h, before purification of amplified template to remove primers and

572   fragments of RNA using QIAquick PCR Purification Kit (QIAGEN), following the

573   manufacturer's instructions. Quantification by measuring absorption at 260nm is

574   confounded by RNA contamination, so dsDNA quantification was performed using a Quant-

575   iT PicoGreen dsDNA Assay Kit (Invitrogen), following the manufacturer's instructions.

576   Fluorescence measurements were taken with a UV-visible spectrophotometer (Molecular

577   Devices, SpectraMax i3).

578   *RT-RPA reaction (final assay with amplification)*: RT-RPA of the template was performed

579   using TwistAmp Basic Kit (TwistDx). The master mix, containing 480nM of forward and

580   reverse primers (for sequences see Extended Data Figure 8d, Integrated DNA Technologies),

581   1x rehydration buffer (TwistDx), reverse transcriptase (M-MLV Reverse Transcriptase,

582   Invitrogen) and nuclease-free water (Invitrogen), was prepared in a tube. For each RPA

583   reaction, 2μL of target HIV-1 RNA template was added to 45.5μL of master mix and a

584   freeze-dried RPA pellet. The reaction was started by adding 2.5μL of magnesium acetate to

585   each reaction, giving a final reaction volume of 50μL. The RT-RPA reactions proceeded at 37

586   °C in a thermal incubator for 10min. The RT-RPA products were purified by QIAquick PCR

587   Purification Kit (QIAGEN) and resuspended in a final volume of 50μL elution buffer for each

588   reaction.

589   *RT-RPA reaction (UCLH clinical standards)*: RNA from the UCLH HIV-1 viral load positive and

590   negative standards (personal communication, gift from Paul Grant, UCLH) was extracted

591   from a 140μL sample using the QIAamp Viral RNA Mini Kit (QIAGEN) essentially according to

592   the manufacturer's instructions, except that elution was in 60μL water. 10μL of extracted

593   RNA in water was used for each RT-RPA reaction.

594   *RT-RPA reaction (seroconversion panel)*: RNA from an HIV-1 seroconversion panel (thirteen

595   samples - ZeptoMetrix Corporation, Panel Donor No. 73698) was extracted from a 140μL

596   sample using the QIAamp Viral RNA Mini Kit (QIAGEN) essentially according to the

23

597   manufacturer's instructions, except that elution was in 60μL water. 2μL of extracted RNA in

598   water was used for each RT-RPA reaction. The RT-RPA reactions proceeded at 37 °C in a

599   thermal incubator for 10.5min. The RT-RPA products were purified by QIAquick PCR

600   Purification Kit (QIAGEN) and resuspended in a final volume of 50μL elution buffer for each

601   reaction.

602   **Lateral flow assay.** The following assays all use LFA strips with a poly-streptavidin test line,

603   blocked by a proprietary polyvinylpyrrolidone-sucrose method (Mologic). The strips were

604   5mm wide with the test line positioned 7mm from the bottom of the strip.

605   A major challenge in developing sensitive LFAs is non-specific binding. To this end, sweeps

606   of running buffers and washing buffers were performed to identify the combination giving

607   the best SBR (see Extended Data Figure 6). This gave rise to a reduction in non-specific

608   binding to the strip, reducing the blanks, and increasing the signal in turn. The optimum

609   buffers in this study were found to be non-fat milk 5wt% + 0.05vol% Empigen in deionised

610   water (running buffer) and 0.2wt% BSA with 0.2vol% Tween 20 in acetate buffer 10mM pH

611   5 (washing buffer).

612   Having chosen running and washing buffers, the background was further reduced by

613   optimising the concentration of FNDs, as shown in Extended Data Figure 7a-b. LFA strips

614   were run with a dilution series of FND concentration. A positive test (500pM of DNA) and a

615   negative control (deionised water) were run at each FND concentration. The fitted

616   relationships between positive and negative lock-in amplitude signals and FND

617   concentration were used, along with modelling of equilibrium binding, depending on

618   antigen and FND concentration. This allowed the estimation of the LODs and dynamic

619   ranges at each FND concentration, as explained in the Extended Data Figure 7c-d and

620   Supplementary Information 2, leading to the selection of the FND concentration. The

621   dynamic range is limited by the total number of FNDs at the top end and the non-specific

622   signal in the negative at the bottom end. The chosen concentration gave a per-strip FND

623   cost of less than 0.02¢ (4.8ng of FNDs per strip). Total cost of consumables per test and

624   estimated costs of a strip reader are shown in Supplementary Table 1.

625   The LFAs were performed by pipetting the solutions to be run into wells of a 96-well plate,

626   then dipping the strips into the wells. All LFAs were performed at room temperature.

627   Purified ssDNA concentrations were measured by absorption using the Nanodrop One^C

628   (Thermo Scientific).

629   *Assay with FND-BSA-biotin*: BSA-biotin-functionalised FNDs were diluted in running buffer

630   to the particle concentrations shown in Extended Data Figure 5d. 55µL of this suspension

631   was run on each LFA strip.

632   *Assay for model RT-RPA products*: Initial optimisation and benchmarking was performed

633   using a model ssDNA RT-RPA 'amplicon' (a short ssDNA strand with digoxigenin and biotin

634   modifications at opposite ends), before moving to real RT-RPA amplicons for the final assay.

635   A comparison of real RT-RPA amplicons with the model ssDNA 'amplicon' is shown in

636   Extended Data Figure 9a, validating its use for optimisation, with similar K_D values and

637   dynamic ranges, although more variation in the blanks with real amplicons gives a higher

638   LOD. A Monte Carlo simulation of the variances of the clinical sample lock-in amplitudes

639   that can be explained by FND size distribution gives a value of ~8–9% of the total variance

640   (Extended Data Figure 9d). A further ~0.1–2% of variance is explained by periodic drift in

641   the modulation amplitude (Extended Data Figure 9e), and frequency noise contributes

642   negligible variation (Extended Data Figure 9f), indicating that the majority is from other

643   factors, such as strip-to-strip inconsistency. This strip-to-strip variation is more evident with

644   larger FNDs, which could be because they are close to the minimum pore size of the

645   nitrocellulose. LODs for the three FND diameters using the model ssDNA 'amplicon' is

646   shown in Extended Data Figure 9b.

647   A single strand of DNA (26 bp), functionalised with digoxigenin at the 3$'$ end and biotin at

648   the 5$'$ end (Integrated DNA Technologies, 5$'$ biotin-GTCCGAGCGTACGACGAACGGTCGCT-

649   digoxigenin 3$'$) was used as a model for RT-RPA amplicons produced with biotin and

650 digoxigenin functionalised primers. These model ssDNA strands were diluted in running

651 buffer and 50µL of this solution was mixed with 5µL of anti-digoxigenin antibody-

652 functionalised FND suspension (1,400, 170 and 3fM in PBS for 120, 200 and 600nm

653 diameters, respectively). After 10min at room temperature, these solutions were run on

654 LFA strips. After all the solution was run (approximately 10min), the strips were transferred

655 to wells of a 96-well plate with 75µL of washing buffer (~12min).

656 *Assay for real RT-RPA products (amplicon serial dilution)*: After purification and

657 quantification of amplicons, the assay was run and washed identically to the model RPA

658 products above with FND concentrations of 2,600, 120 and 4fM for 120, 200 and 600nm

659 diameters, respectively.

660 RT-RPA used a digoxigenin-modified forward primer and a biotin-modified reverse primer.

661 The RT-RPA products, therefore, consist of dsDNA (181bp), each copy including a

662 digoxigenin molecule at one end and a biotin molecule at the other. These modifications

663 bind to anti-digoxigenin-functionalised FNDs, and the poly-streptavidin test line on the

664 nitrocellulose paper, respectively, forming a sandwich structure and immobilising FNDs in

665 the presence of amplicons, as shown in Figure 4a.

666 *Final assay for RNA quantification with RT-RPA*: After purification, 10µL of 6X running buffer

667 (30wt% non-fat milk with 0.3vol% Empigen in deionised water) was added to the 50µL RT-

668 RPA product. 5µL of anti-digoxigenin antibody-functionalised FND suspension was added

669 before running the strips as above. For the lowest positive sample (average of 1.26 copies),

670 there is a 71% chance of having at least one copy, based on the Poisson distribution. This

671 gives a 26% chance of all four experimental replicates having at least one copy, using the

672 binomial distribution, and a 42% chance for three of the four replicates. For the next

673 dilution (average of 0.13 copies), these probabilities fall to 0.019% and 0.60%. These

674 probabilities are consistent with the results in Figure 4.

675 Fluorescence Modulation and Imaging. The paper strips were imaged using a fluorescence

676 microscope (Olympus BX51) with a 550nm green LED as excitation light source (pE-4000,

677   CoolLED), with a filter cube containing an excitation filter (500nm bandpass, 49nm

678   bandwidth, Semrock), a dichroic mirror (596nm edge, Semrock) and emission filter (593nm

679   long-pass, Semrock). A 20x/0.4 BD objective (LMPlanFl, Olympus) was used. Images were

680   recorded with a high-speed camera (ORCA-Flash4.0 V3, Hamamatsu) using HCImage Live

681   software (Hamamatsu).

682   All strips were measured when dry to eliminate any possible variation due to drying during

683   measuring. Extended Data Figure 12 shows the detection on wet strips and the effect of

684   drying on the lock-in amplitude of the FND signal. This experiment was performed by

685   running positive and negative LFAs with the model 'amplicon' as above, then fixing each

686   strip to the microscope stage directly after completing the wash step. A 15-second lock-in

687   measurement at an exposure time of 20ms was taken every 1min. The light source was only

688   on during measurement to prevent it speeding up drying. One of the negative controls was

689   measured for less than 55min (35min), so its mean was used after this time in Extended

690   Data Figure 12. There is a small loss in sensitivity on wet strips ($\sim$1.4–1.9x), corresponding

691   to a necessary increase in isothermal amplification time of less than 1min.

692   A microwave field was generated by a voltage controlled oscillator (VCO, Mini-Circuits,

693   ZX95-3360+) and a low noise amplifier (Mini-Circuits, ZX60-33LN+) connected to the

694   resonator circuit board (Minitron Ltd, Rogers 4003C 0.8mm substrate and 1ozft^{-2} copper

695   weight). The resonator was attached to the microscope stage. The tuning voltage of the

696   VCO was set to maximise the decrease in fluorescence. Modulation of the signal was

697   achieved by modulating the input voltage of the VCO with an on-chip reference frequency

698   generator at 4Hz using a

699   32.768kHz crystal oscillator (DS32KHZ, Farnell Ltd) with a 14-stage frequency divider

700   (CD4060BM, Farnell Ltd). Circuit board design was performed using EAGLE (Autodesk). A

701   sweep of modulation frequencies was performed using this VCO and amplifier, using a

702   microcontroller (Arduino Nano 3.0) to generate the different modulation frequencies.

703 The power dependence of the decrease in fluorescence was recorded using a benchtop

704 microwave generator (HM8135, Rohde & Schwartz Hameg) and a low noise amplifier (Mini-

705 Circuits, ZRL-3500+). A broad sweep of microwave frequencies was measured with RF signal

706 generator (WindFreak Technologies LLC, SynthUSBII).

707 **Computation lock-in and LOD.** The fluorescence signal was modulated with a set

708 modulation frequency (F_m) and the amplitude of the resulting signal was computed with a

709 computational lock-in algorithm. Images were recorded with the high-speed camera (ORCA-

710 Flash4.0 V3, Hamamatsu) at a sampling frequency F_s. Each frame was averaged to get a

711 mean pixel value at each time point $t_0 = 0$ to $t_L = L/F_s$, where L was the total number of

712 frames. A moving average low-pass filter with a span width of $1.5 \cdot F_s/F_m$ was applied to the

713 fluorescence time series. The filtered signal, V_{in} was multiplied by two reference signals: in-

714 phase ($\sin(2\pi F_m t)$) and $\pi/2$ out-of-phase ($\cos(2\pi F_m t)$) to obtain V_x and V_y, respectively:

$$V_x = V_{in} \cdot \sin(2\pi F_m t) \tag{3}$$

$$V_y = V_{in} \cdot \cos(2\pi F_m t) \tag{4}$$

715 The DC components of these two signals, X and Y, were calculated by finding the mean of V_x

716 and V_y, respectively, and enabled the evaluation of the magnitude R of the lock-in

717 amplitude at the frequency F_m according to:

$$R = \sqrt{X^2 + Y^2} \tag{5}$$

718 Where there was no FND saturation (BSA-biotin assays), the LOD was computed by fitting

719 the lock-in amplitude, as a function of concentration, c, to a linear regression. Where there

720 was saturation, (all assays except BSA-biotin assays) a Langmuir isotherm was fitted:

$$SBR = k_0 + k_1 \cdot \frac{[T]}{K_D + [T]} \tag{6}$$

721   where k_0 is SBR of the negative control, k_1 is a scaling constant representing the SBR at

722   target saturation, [T] in the amplicon concentration, and K_D is the equilibrium dissociation

723   constant. Fitting was performed in Matlab using the fitlm and nlinfit functions for linear and

724   Langmuir fits, respectively, weighting the fit by the variance at each concentration.

725   The LOD was defined as the intersection of the lower 95% confidence bound of the fit with

726   the upper 95% confidence bound of the blank measurements.[41]

Methods References

728   51. Kim, E. Y. *et al.* A real-time PCR-based method for determining the surface coverage of

729   thiol-capped oligonucleotides bound onto gold nanoparticles. *Nucleic Acids Research* **34**, 1–

730   7 (2006).

731   52. Besnier, C., Takeuchi, Y. & Towers, G. Restriction of lentivirus in monkeys. *Proceedings of*

732   *the National Academy of Sciences of the United States of America* **99**, 11920–11925 (2002).

733   53. Bainbridge, J. W. *et al.* In vivo gene transfer to the mouse eye using an HIV-based lentiviral

734   vector; efficient long-term transduction of cornealendothelium and retinal pigment

735   epithelium. *Gene Therapy* **8**, 1665–1668 (2001).

736   54. Foley, B. *et al.* HIV Sequence Compendium 2017 Editors. *Eds. Published by Theoretical*

737   *Biology and Biophysics Group, Los Alamos National Laboratory, NM, LA-UR 18-25673*

738   (2017).

739   55. Kong, J. & Yu, S. Fourier transform infrared spectroscopic analysis of protein secondary

740   structures. *Acta Biochimica et Biophysica Sinica* **39**, 549–559 (2007).

741   56. Zadeh, J. N. *et al.* NUPACK: Analysis and design of nucleic acid systems. *Journal of*

742   *Computational Chemistry* **32**, 170–173 (2011).

743 57. SantaLucia, J. A unified view of polymer, dumbbell, and oligonucleotide DNA nearest-

744 neighbor thermodynamics. *Proceedings of the National Academy of Sciences of the United*

745 *States of America* **95**, 1460–5 (1998).

746 58. Laitinen, M. P. & Vuento, M. Affinity immunosensor for milk progesterone: Identification of

747 critical parameters. *Biosensors and Bioelectronics* **11**, 1207–1214 (1996).

748 **Data Availability**

749 The datasets generated during and/or analysed during the current study, and the computer

750 code used are available from the corresponding author on reasonable request, in line with

751 UCL and funder's requirements (EPSRC policy framework on research data).

752 **Extended Data Captions**

753

754 **Extended Data Figure 1: Optimisation of microwave modulation.** A linear resonator was designed

755 to have a wideband response over the range 1–4GHz, and an omega narrowband resonator was

756 designed to have a stronger, narrower resonance at 2.87GHz with quality factor Q = 100. The

757 schematic printed circuit board layouts for the two resonators are shown in (a) and (d), respectively.

758 The resulting simulated fields are shown in (b) and (e), respectively. The reflected power (S11) is

759 plotted against frequency in (c) and (f). The narrowband resonator shows 5-6 orders of magnitude

760 greater absorption than the wideband resonator at 2.87GHz, indicating resonant coupling giving

761 strong absorption. (f) Also shows the corresponding FND intensity dip. (g) Emission spectra of FNDs

762 acted on by a 2.87GHz microwave field. The powers listed in decibel-milliwatts are the output power

763 of the microwave generator (before the 17dB amplifier). (h) Each spectrum is integrated over the

764 whole wavelength range to give a total intensity, which is plotted against preamplifier power. This

765 shows a linear relationship between fluorescence intensity and microwave power (in dBm) above a

766 threshold power, and up to 7dBm, where the amplifier reaches its 1dB compression power. At this

767 point, the fluorescence starts to increase again due to a loss in the quality of the sinusoid leading to

768 power lost in harmonics. Error bars show the standard deviations, with 3 measurement repeats (n_M

769 = 3).

770

771 **Extended Data Figure 2: Optimisation of lock-in analysis.** (a) Schematic of the computational lock-in

772 algorithm used to extract the microwave modulated FND signal from the background. The input

773   signal is high-pass filtered using a moving average filter to remove low-frequency drift. It is

774   subsequently multiplied by cosine and sine functions with frequency F_m, and the resulting signals are

775   low-pass filtered to generate the in phase and quadrature components, respectively, of the vector

776   representation of the signal. The magnitude of this vector is calculated to remove the effect of

777   phase, giving the output magnitude. (b) The variation of lock-in amplitude with modulation rate (F_m)

778   at various sampling rates (F_s). A single strip with very high intensity was modulated at F_ms between

779   1–450Hz, and sampled at various F_ss between 3.89–996Hz. The resulting plot shows that lock-in

780   amplitude is independent of F_s when $F_s > 2F_m$. (c) and (d) show the relationships between lock-in

781   amplitude, exposure time (T_e) and modulation frequency (F_m). An identical LFA strip was measured

782   with exposure times between 10–50ms, using the maximum possible F_s for each T_e, and F_ms

783   between 1–15Hz. (d) shows F_m against lock-in amplitude at various exposure times. It is shown that

784   the lock-in amplitude has its maximum ~5Hz for all frequencies, and reduces when F_m is close to

785     $F_s/2$, its maximum possible value. This is evident in the raw signal plots in (c) for each F_m at a fixed

786   exposure time of 30 ms. As F_m approaches $F_s/2$, the sampling effects obscure the square wave,

787   decreasing lock-in amplitude. For maximum lock-in amplitude, the highest possible T_e should be

788   used. Here, we are limited to 50ms by the background autofluorescence of the nitrocellulose, which

789   saturates the camera above this value. A corresponding F_m of 4Hz was chosen as it is in the optimal

790   range and is a power of 2, so can be achieved by simply dividing the temperature compensation

791   crystal oscillator (TCXO) frequency. (e) The variation of lock-in amplitude with total measurement

792   time at $F_m = 4$Hz and $F_s = 20$Hz for five different concentrations of FNDs and a negative control,

793   immobilised with a biotin-avidin interaction. The positive amplitudes stabilise quickly, reaching 5%

794   of their 15s value in 3.9s for positive results. The negative results take longer to stabilise, reaching

795   5% of their 15s value in 13s. A measurement time of 15s (300frames) was used for subsequent

796   measurements. (f) Schematic circuit design of temperature compensation crystal oscillator (TCXO)-

797   based modulated microwave source. It is powered by a 5 V source which powers a TCXO, which

798   outputs a 32.768kHz square wave. This is converted to a 4 Hz signal by a 4060 counter chip. This

799   square wave controls two transistors which deliver 12 V stepped up power (DC converted) to the

800   microwave VCO. The bias voltage is regulated from 12 V to 8.15 V by a voltage regulator. The VCO

801   microwave output is amplified by the MW amplifier and transmitted to the omega resonator. (g)

802   Printed circuit board layout of the prototype (65mm x 38mm). Outputs for the microwave amplifier

803   and microwave VCO are at the top right and bottom right, respectively. A photo of the printed

804   circuit board with a pound coin for scale is shown below.

805

806   **Extended Data Figure 3: FND characterisation and functionalisation.** (a) Comparison of the

807   nonspecific binding of various commercial FNDs with various surface functionalisations on LFAs. The

808   lock-in amplitude at the test line was measured to quantify non-specific binding. The LFAs were also

809   pre-blocked with a polyvinylpyrrolidone-sucrose solution (proprietary method, Mologic). The lowest

810   non-specific binding was from the PG-functionalised particles (FND-PG), as the PG adds a hydrophilic

811   layer. (b) Dynamic light scattering of three different FND particle core diameters: 120, 200 and

812   600nm. (c) A schematic of antibody functionalisation of FND-PG. Disuccinimidyl carbonate (DSC)

813   activates hydroxyl surface groups to form succinimidyl carbonates, which can then react with

814   antibodies to form stable carbamate or urethane bonds. (d)-(f) show scanning electron microscope

815   images of FNDs with particle core diameters of 120, 200 and 600nm, respectively. (g) Dynamic light

816   scattering was also used to measure the size and aggregated fraction after functionalisation of

817   120nm FND-PG before and after functionalisation with BSA-biotin or antibodies. Fitting the number

818   plots to skew exponentials (Equation 3 in methods) gave peak particle hydrodynamic diameters of

819   106, 121 and 128nm. (h) The fitted peak diameters are plotted with error bars denoting their 95%

820   confidence intervals, showing no significant difference between the bio-functionalised diameters

821   (FND-Biotin, FND-Ab), but both are significantly different from the pre-functionalisation diameter

822   (FND-PG): * indicates a p-value of ≤0.05 and ** a p-value of ≤0.01 using a Tukey HSD post-hoc test.

823   (i) FTIR spectroscopy of FND-PG and antibody-functionalised FND-PG. C-O and C-H peaks, indicative

824   of the PG layer can be seen in both FND-PG and FND-PG-antibody at $\sim$1,100cm^{-1} and $\sim$2,900cm^{-1},

825   respectively. The FND-PG-antibody spectrum displays additional peaks at $\sim$1,640cm^{-1} and

826    $\sim$1,540cm^{-1}, suggesting protein Amide I and Amide II bonds, respectively[55], showing that protein

827   functionalisation was successful.

828

829   **Extended Data Figure 4: Quantification of the number of available binding sites per FND.** (a)

830   Initially, binding constants of the anti-digoxigenin (anti-DIG) antibody binding to DIG were measured

831   using interferometry. Full experimental details are shown in Supplementary Information 1. Binding

832   at different concentrations was measured and the resulting curves were fitted to exponentials. To

833   find the equilibrium dissociation constant (K_D), equilibrium binding values, B, were plotted here

834   against concentration, C. A Langmuir adsorption isotherm was fitted ($B^{\infty} = \frac{a \cdot C}{K_D + C}$) giving a K_D value

835   of 5.1×10^{-10} M. (b) In order to find the on- and off-rates, k_{on} and k_{off}, the observed reaction rates,

836   k_{obs}, at each concentration were plotted and fitted to the linear relationship: $k_{obs} = k_{off} + C \cdot k_{on}$. The

837   resulting fitted values are $k_{on} = 1.6 \times 10^5$ M^{-1}s^{-1} and $k_{off} = 9.1 \times 10^{-5}$ s^{-1}. (c) A schematic of the assay to

838   quantify the number of available binding sites per FND. After functionalisation of FNDs with anti-DIG

839   antibodies, a $\sim$50-fold excess of DIG-modified DNA was added and left to bind for 2h. The negative

840   DNA control used the same sequence, but with no DIG modification to compensate for non-specific

841   binding and adequate washing. After multiple washes by centrifugation to remove the excess DNA,

842   the remaining DNA (bound to FNDs) was quantified by qPCR. See Extended Data Figure 8d for

843   template, primer and probe sequences, and Methods for full experimental details. (d) A kinetic

844   binding simulation was performed to verify that all available sites would be occupied after 2h with

845   the above excess. The graph shows the fraction of sites on the FNDs which are occupied, with this

846   ∼50-fold excess, over a range of K_D, k_{on} and k_{off} values. The red cross in circle marks the location of

847   the anti-DIG antibody used in this paper (using the values measured in (a) and (b)), indicating that

848   >99.9% of available sites will be occupied after 2h. This means that quantifying the DNA gives a true

849   measure of available binding sites. (e) Amplification plot showing the normalised fluorescence

850   intensity against number of cycles. A standard curve of each decade from 40 copies to 4×10^8 copies

851   is plotted, along with the sample and negative control FND samples described above. The negative

852   diluent controls are also plotted along with the C_q threshold. The shaded areas show the standard

853   deviation of repeats ($n_T = 3$ for standard curve and $n_T = 6$ for samples). (f) The resulting C_q values are

854   plotted against copy number per reaction. Error bars show standard deviations ($n_T = 3$ for standard

855   curve and $n_T = 6$ for samples). The standard curve was fitted to a logarithmic curve ($C_q = -3.2\log_{10}$

856   *copies* + 39), allowing calculation of the number of copies in the DIG-DNA sample and negative DNA

857   control. Dividing by the particle concentration (measured as shown in Extended Data Figure 5c) and

858   subtracting the negative DNA control value, gives the number of available binding sites per particle

859   as 4,300 sites. This is within what is geometrically plausible, giving an area per antibody of at least

860   200nm^2 (assuming at least 1 paratope available of at least 75% of the bound antibodies). The

861   corresponding calculated values for 120 and 200nm particles are 172 and 477 available binding sites

862   per FND respectively, assuming the same loading density.

863

864   **Extended Data Figure 5: Lateral flow and FND benchmarking.** (a) Measurement of flow rate of

865   lateral flow strips. During wetting, the flow follows the Washburn equation, where $V \sim t^{\frac{1}{2}}$ (inset), and

866   during fully-wetted flow, Darcy's law for capillary flow is followed ($V \sim t$), with a constant flow rate

867   of 6.9µLmin^{-1}. (b) Using a one-to-one receptor-ligand binding approximation, the binding of

868   biotinylated FNDs to streptavidin was modelled kinetically, indicating that all the FNDs bind with a

869   residency time of $> \sim 10^{-3}$ s. Here, the residency time is measured as 4s, using the flow rate from (a),

870   so all the FNDs should bind. (c) An example of the measurement of FND concentration. FND

871   fluorescence is unaffected by surface chemistry, so is used to quantify concentration. A serial

872   dilution of FND suspensions was performed, from a known stock concentration (filled circles with

873   error bars showing standard deviations). This was then fitted with a linear regression (lines) to find a

874   relationship between fluorescence intensity and concentration. After each FND functionalisation,

875   the final suspensions' fluorescence intensities were measured, and the linear fit was used to

876   estimate concentration (crosses). (d) Fundamental LODs for different size FNDs on LFAs, using a

877   model biotin-avidin interaction. 55µL suspensions of BSA-biotin-functionalised FNDs were run at

878   different concentrations on poly-streptavidin strips. Concentrations were chosen to span the

879   dynamic range of the camera, limited by over-exposure, as seen with the top concentration of 200

880   and 600nm FNDs. Error bars show standard deviations (n_T = 3, n_M = 3). Each series is fitted to a

881   simple linear regression, shown as the solid line, with 95% confidence intervals shown shaded. LODs

882   for 120, 200 and 600nm diameter FNDs are 200aM, 46aM, and 820zM respectively, defined by the

883   intersection of the lower 95% confidence intervals of the linear fit with the upper 95% confidence

884   intervals of the blanks for each particle size.

885

886   **Extended Data Figure 6: Assay optimisation by buffer selection.** Sensitivity is limited by the

887   nonspecific binding of FNDs at the LFA test line. LFA strip blocking, running buffer and washing step

888   are, therefore, key factors in improving LOD. In this section 120nm FNDs were used for optimisation.

889   (a) Signal-to-background comparison for the in different running buffers. There is no wash step.

890   Error bars show standard deviations (n_M = 3). Milk was selected as the basis for the running buffer.

891   (b) Subsequently, a sweep of different surfactants was performed (n_M = 1). The best signal-to-

892   background ratio came from adding 0.05vol% Empigen, showing a significant increase in the signal-

893   to-background. There is no wash step. (c) The best running buffer was then used for a washing

894   buffer pH sweep (n_M = 1). All washing buffers were run at a volume of 75µL, chosen because

895   preliminary experiments showed it to be a good compromise between assay time and washing

896   success. Although results were similar, pH 5 gave the best signal-to-background ratio, so acetate

897   buffer at 10mM pH 5 was used as the basis for a second washing buffer sweep, shown in (d), testing

898   a number of detergents and adding casein at 0.2wt% as a blocking protein (n_M = 1). As a final test,

899   the three best running buffers were tested, each with the three best washing conditions, displayed

900   as a grid in (e). Each square is the average of three measurements (n_M = 3). The results were

901   consistent with previous sweeps, the combination of the best running buffer and best washing

902   buffer giving the best signal-to-background. Milk and protein percentages are by weight and

903   detergent percentages are by volume.

904

905   **Extended Data Figure 7: Optimisation of FND concentration.** The background was reduced by

906   optimising the particle concentration, shown here for 120nm FNDs. (a) A positive LFA strip (500pM

907   of ssDNA) and a negative control (deionised water) were run at varying FND concentrations

908   between 3.88fM and 496fM, plotted against FND concentration, and fitted to simple linear
909   regressions. The error bars show the standard deviations of repeat measurements (n_M = 3). Linear
910   regressions are shown by solid lines, and shaded areas show the 95% confidence intervals of the fits.
911   (b) Signal-to-background ratio, found by dividing the fitted linear regressions in (a), is plotted against
912   FND concentration. At higher concentrations, where the gradient term of the linear regression
913   dominates, the positive and negative lock-in values tend to a constant separation on the log-log
914   plot, so the signal-to-background ratio tends to a constant value of ~27. At low concentrations, the
915   positive and negative curves converge as the negative lock-in amplitude levels off at the noise
916   threshold, and the signal-to-background ratio tends to 1. (c) The fitted linear regressions in part (a)
917   were used, along with the antibody equilibrium dissociation constant measured in Extended Data
918   Figure 4, to estimate the variation of lock-in amplitude with analyte concentration at different FND
919   concentrations. The principles and equations are described in full in Supplementary Information 2.
920   The LOD for each FND concentration is defined as the intersection of this plot with the value of the
921   blank plus two times the 95% confidence interval at that value, assuming a low concentration
922   positive would have a similar confidence interval. (d) The estimated LODs and dynamic ranges from
923   (c), plotted against FND concentration, to determine the optimum.

924

925   **Extended Data Figure 8: Primer Optimisation.** (a) List of forward primers (F1–F5) and reverse
926   primers (R1–R5) tested for the initial primer screen. (b) An initial primer screen was performed to
927   achieve the highest amplification efficiency (n_T = 3) using the TwistAmp Exo Reverse Transcription Kit
928   (TwistDx). The yield of each primer combination was measured by the fluorescence of the exo probe
929   with a fluorescence microplate reader (SpectraMax i3, Molecular Devices LLC). Primers F5 and R3
930   gave the highest yield, although all the yields were above 63% of this value. (c) Interactions between
931   forward primers and reverse primers to predict the minimum free energy structures for the ten
932   primer combinations that gave the largest yield of RPA product in the primer screen. The table
933   shows the results of simulations in NUPACK[56], using an input of 10µM for each oligonucleotide. The
934   minimum free energy secondary structures are the most energetically favourable secondary
935   structures that can be assumed for oligonucleotides of a given primary sequence, calculated using
936   the nearest-neighbour method[57]. Primers F1 and R4 were selected for future work since the
937   energetics of their hybridisation are much less favourable than that of F3 and R5, yet they still gave
938   a high RPA yield in the primer screen (93% of the highest yield pair). (d) A list of oligonucleotides
939   used for PCR, RPA and qPCR assays. The PCR reverse primer included a T7 promoter for RNA
940   transcription (underlined) and a spacer (bold). (e) Gel electrophoresis of 1,503bp template sequence

941   produced by PCR using a 1% agarose gel. (f) Gel electrophoresis of 181bp double-stranded RT-RPA

942   products using a 1% agarose gel.

943

944   **Extended Data Figure 9: Comparison of LODs of model ssDNA with real RPA amplicons and gold**

945   **nanoparticles.** (a) The dilution series of the real RPA amplicons and the model ssDNA 'amplicons'

946   were plotted against concentration for 600nm FNDs (dots with error bars showing standard

947   deviations, n_T = 3-9, n_M = 3) with their respective linear fits (solid lines with 95% confidence intervals

948   of the fit shown shaded). The curves are similar, with fitted K_D values of 29 and 22fM for model and

949   real amplicons, respectively, and similar dynamic ranges. The real amplicons showed increased

950   variation in the blanks, leading to a higher blank cutoff giving a higher LOD, and slightly reduced

951   signal-to-blank ratio. (b) The dilution series of model ssDNA 'amplicons' were plotted against

952   concentration for 120, 200 and 600nm FNDs (dots with error bars showing standard deviations, n_T =

953   3, n_M = 3) with their respective linear fits (solid lines with 95% confidence intervals of the fit shown

954   shaded). The LODs are 3.7, 3.6 and 0.8fM respectively. (c) Comparison of 600nm FNDs with 40nm

955   gold nanoparticles on LFAs, commonly used in LFAs due to a good compromise between stability

956   (and therefore ease of functionalisation), and sensitivity[58]. Serial dilutions are plotted (dots with

957   error bars showing standard deviations, n_T = 3, n_M = 3 for the FNDs; and dots with error bars showing

958   the standard deviations across the test line, n_T = 1, n_M = 1 for the gold nanoparticles) LODs are

959   calculated as previously, giving 800aM and 6.0pM, respectively. (d) A Monte Carlo simulation of the

960   signal variation that can be explained by the FND size distribution (from DLS measurements in

961   Extended Data Figure 3b) was performed (n = 200,000). The violin plots show the normalised

962   simulated random variation in lock-in amplitudes due to the 600nm FND size distribution in the

963   clinical sample assays in Figure 4d (negative plasma control and clinical standard). The experimental

964   data is overlaid, showing that FND size distribution explains ∼8–9% of the total experimental signal

965   variance. A further ∼0.1–2% of the variance is explained by periodic drift in modulation amplitude,

966   shown over 45min in (e), normalised to the mean. (f) shows a plot of the variation in lock-in

967   amplitude due to small changes in the modulation frequency, F_m. The variance of the frequency is 3

968    $\times 10^{-8}$% over the same period, giving negligible differences in lock-in amplitude. Full details of the

969   simulation are given in Supplementary Information 3.

970

971   **Extended Data Figure 10: Further analysis of RT-RPA samples.** (a) ANOVA analysis was performed

972   on the measured lock-in amplitudes of the FND LFAs, giving a *P* value of 7.4×10^{-29} and F value of

973   95.6, with 71 total degrees of freedom. Box plots of the data groups are shown (grouped by RNA

974   concentration). The horizontal red lines represent the medians, the horizontal blue lines represent

975   the 25th and 75th percentiles and the notches represent the 95% confidence intervals of the

976   medians. The black dashed lines represent the range for each group. (b) A graphical comparison of

977   the means of the groups (grouped by RNA concentration). The circles represent the means, and the

978   horizontal lines represent the comparison intervals of the means (overlap of these intervals denotes

979   statistical similarity). The negative control, highlighted in blue, is shown to be not significantly

980   different from the 10^{-2} and 10^{-1} RNA copy number samples (*P* values >0.999, shown in grey), but it is

981   significantly different from the 1, 10^1, and 10^2 RNA copy number samples (*P* values ~10^{-8}, shown in

982   red). (c) A table of ANOVA *P* values. The *P* value for the null hypothesis that the difference between

983   the means of the two groups is zero. (d) Comparison of amplification time for a low copy number

984   RT-RPA sample (average of 1.26 RNA copies). Multiple RPA reactions were run and stopped after

985   different times, before adding to FND LFAs, as described in methods. A negative control is shown for

986   comparison, and the dashed line represents the upper 95% confidence interval of the negative

987   control. Dots show the mean of the measurement repeats (n_M = 3), crosses show the individual

988   measurements, and error bars represent the standard deviation. (e) Early disease detection using

989   FND LFAs was demonstrated by a seroconversion panel (ZeptoMetrix Corporation, Panel Donor No.

990   73698), taken from a single donor over a period of six weeks spanning the early stages of an HIV-1

991   infection. The thirteen samples of the panel were measured on FND LFAs (n_E = 1 − 2, n_M = 3). The

992   measured values are plotted along with positive and negative non-amplification controls. They are

993   colour-coded for RT-PCR results, and labelled with sample numbers, dates, and copy numbers in

994   brackets. The blank cutoff is defined as the upper 95% interval of the negative control. The results

995   show that the RNA was detectable on FND LFAs as early as RT-PCR, and 6/7 RT-PCR-positive samples

996   were detected on FND LFAs, whilst 6/6 RT-PCR-negative samples were negative.
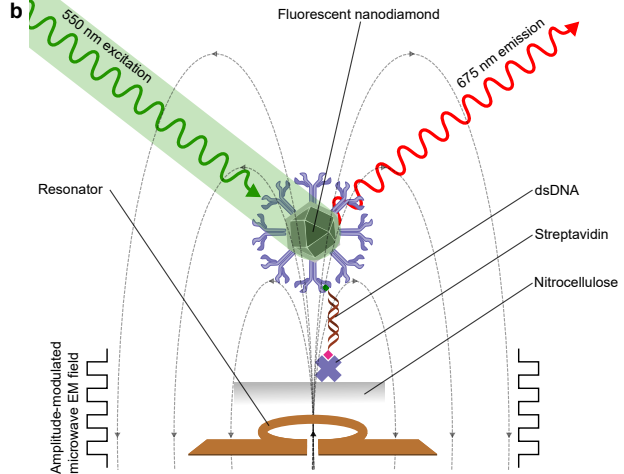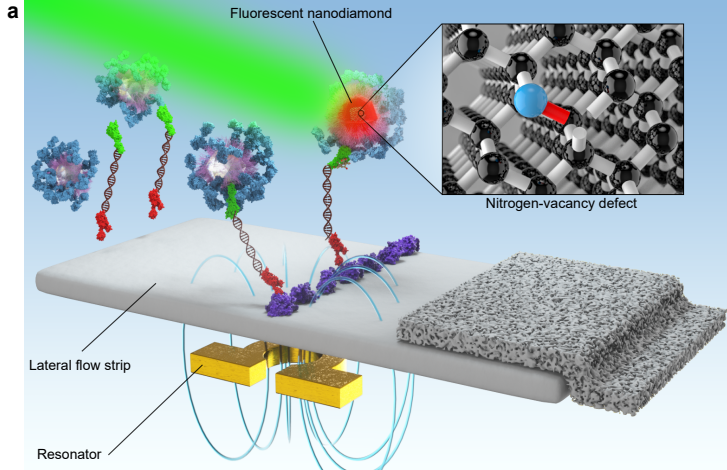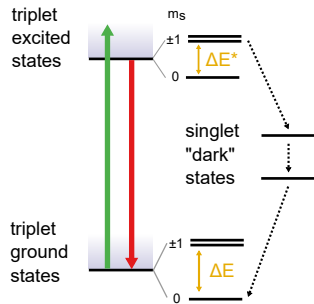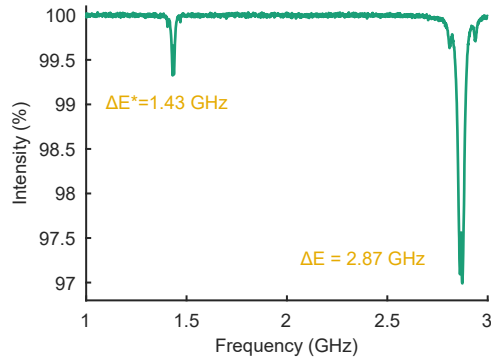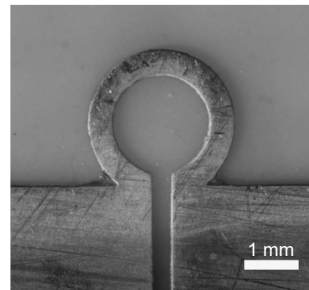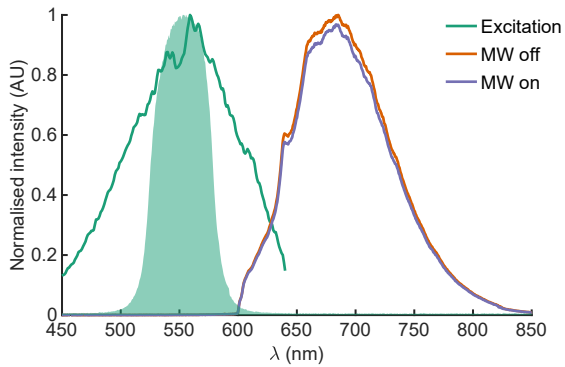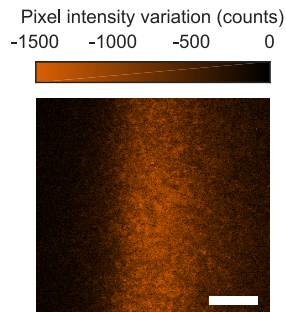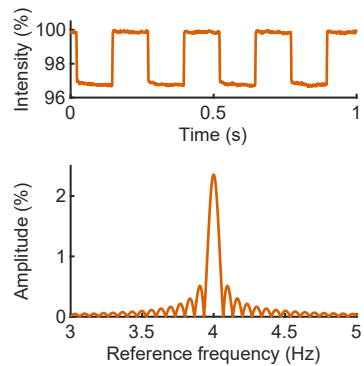
997

998   **Extended Data Figure 11: Detection of HIV-1 capsid protein on using 600nm FNDs.** A serial dilution

999   of the capsid protein was detected on streptavidin-modified LFAs using a sandwich of a biotinylated

1000   capture nanobody and antibody-modified FNDs. The results are plotted (n_E = 3 − 4, n_M = 3),

1001   normalised to the blanks for each sample set, and fitted to a Langmuir curve (Methods Equation 6).

1002   This gives a LOD of 120fM, and a lowest concentration that is significantly different from the blank

1003   (at the 95% confidence level) of 3pM, marked with *. Full experimental details are shown in

1004   Supplementary Information 4.

1005

1006   **Extended Data Figure 12: Effect of lateral flow test strip drying on lock-in amplitude of FND assay.**

1007   (a) Positive and negative lateral flow test strips were measured over time after completed running

1008   (time = 0), showing a small increase in the positive strip lock-in amplitude as the strip dries (the

1009   initial lock-in amplitude is ~70% of the final value), however no increase is seen in the negative

1010   control. The shaded areas show the standard deviation between repeats (n_T = 3). (b) The resulting

1011   signal-to-blank ratio variation over time. The shaded areas show the standard deviation between

1012   repeats (n_T = 3), showing that the effect of drying is quite small compared to strip-to-strip variation.

a

Fluorescent nanodiamond

Nitrogen-vacancy defect

Lateral flow strip

Resonator

b

550 nm excitation

Fluorescent nanodiamond

675 nm emission

Resonator

dsDNA

Streptavidin

Nitrocellulose

Amplitude-modulated microwave EM field

a NV⁻ Center

b

$\Delta E^* = 1.43$ GHz

$\Delta E = 2.87$ GHz

c 1 mm

d Excitation / MW off / MW on

e Pixel intensity variation (counts)
−1500 −1000 −500 0

f

a

FND-BSA-Biotin

Streptavidin

Paper

b

- FND lock-in
- FND intensity analysis
- Gold nanoparticles

820 zM   84 aM   81 fM
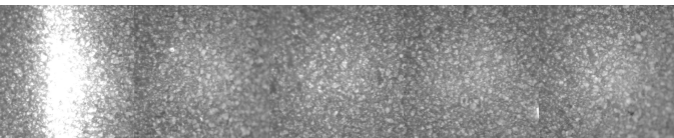
Signal-to-blank ratio

FND Concentration (M)

c

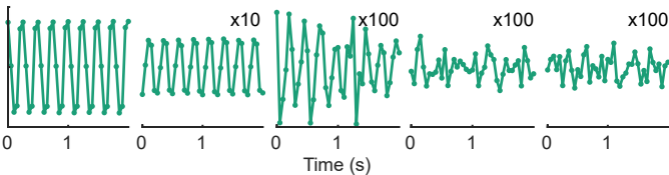FND Concentration

1.8 fM   70 aM   2.8 aM   110 zM   0 M

Fluorescence images

Signal modulation (pixel variation)

x10   x100   x100   x100

Time (s)

a

Virus in patient sample

ssRNA extraction

DNA primer binds to viral ssRNA

Reverse transcription

10-minute RPA followed by purification

Primer binds to complementary DNA

RPA amplicons DIG-dsDNA-biotin

FND-anti-DIG

Streptavidin

Paper

b

- 120 nm
- 200 nm
- 600 nm

9.0 fM
7.5 fM
3.7 fM

Signal-to-blank ratio

DNA concentration (M)

c

Signal-to-blank ratio

RNA copies

d

Signal-to-blank ratio

Water Control   Negative Plasma   Clinical Standard